Additive Manufacturing 124 (2026) 105228

Contents lists available at ScienceDirect

Additive Manufacturing

journal homepage: www.elsevier.com/locate/addma

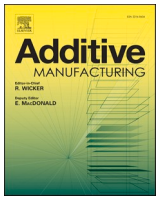

In-situ qualification of lattice structures in L-PBF: A framework for robust geometrical deviation detection

Marco Grasso [a,*], Dimitrii Ertelthalner-Nikolaev [b], Michael Dallmann [c], Bianca Maria Colosimo [a]

[a] Dipartimento di Meccanica, Politecnico di Milano, Via La Masa 1, Milan 20156, Italy
[b] Siemens AG, Otto-Hahn-Ring 6, Munich 81739, Germany
[c] Siemens AG, Gleiwitzer Str. 555, Nuernberg 90475, Germany

ARTICLE INFO

Keywords:
Additive manufacturing
In-situ monitoring
In-situ inspection
Lattice structure
Laser powder bed fusion

ABSTRACT

Part qualification and process verification account for a substantial share of production costs in additive manufacturing, particularly for complex geometries that require expensive non-destructive evaluation. In-situ monitoring offers a promising strategy to mitigate these costs by enabling in-situ inspection and real-time anomaly detection. This study advances the development of industrial solutions for in-situ detection of geometrical deviations in laser powder bed fusion (L-PBF), with a focus on lattice structures as a representative class of complex geometries. From an industrial perspective, the literature reveals two main gaps: (i) the need for systematic calibration of image segmentation algorithms to improve in-situ reconstruction accuracy, and (ii) the lack of clear criteria for selecting deviation metrics that effectively capture actual geometrical defects. This work addresses both issues and provides practical guidelines for implementation. Specifically, we demonstrate that appropriate calibration settings make powder-bed image segmentation robust to variations in illumination and to changes in part size and geometry. In addition, we evaluate the influence of different deviation metrics on inspection performance, identifying those most suitable for reliable industrial use. The approach is validated through a case study on gyroid lattice structures manufactured via L-PBF, where controlled defects of varying severity were introduced to assess detection capability. Defects of varying severity were successfully detected through an appropriate selection of the deviation metric and calibration strategy, while maintaining a false alarm rate below 2%. These results highlight the feasibility of robust in-situ geometrical inspection for industrial applications.

1. Introduction

Ensuring the quality and integrity of additively manufactured parts remains a critical industrial challenge, particularly for complex three-dimensional (3-D) structures and challenging materials. In laser powder bed fusion (L-PBF), defects and geometric deviations can arise due to many different causes, including process instabilities, material inconsistencies, or thermal distortions [16,24,33]. Traditional non-destructive evaluation (NDE) methods like X-ray computed tomography (CT) are costly and time-consuming, which inflates the contribution of part qualification operations to overall production costs. In the presence of intricate internal features, not accessible with other inspection techniques, X-ray CT is the only suitable solution, but it suffers from several limitations, especially in applications involving large components or highly dense materials.

To address these challenges, in-situ monitoring has gained increasing attention as a means of enabling in-line inspection and real-time anomaly detection during fabrication [3,11]. Layerwise imaging with powder-bed cameras—now commonly integrated into industrial L-PBF systems—provides a valuable opportunity for this purpose. By combining readily available in-situ sensors with advanced image processing and monitoring techniques, it becomes possible to gain meaningful insights into process stability and part integrity, thereby reducing reliance on extensive post-process evaluations.

A growing body of research has proposed in-situ inspection methods that exploit post-exposure powder-bed images for geometry reconstruction and anomaly detection on a layer-by-layer basis [28,9,14,27,15,18,34,7,2]. Within this research stream, however, lattice structures,

* Corresponding author.
E-mail address: Marcoluigi.grasso@polimi.it (M. Grasso).

https://doi.org/10.1016/j.addma.2026.105228
Received 1 December 2025; Received in revised form 23 March 2026; Accepted 4 May 2026
Available online 5 May 2026

an important class of 3D geometries for AM adoption across multiple industrial sectors, have received limited attention [19,32]. Colosimo et al., [10] introduced a seminal concept for in-situ inspection tailored to lattice structures: modeling the deviation between reconstructed and nominal areas for each unit cell, thereby compressing the original stack of layerwise images into a set of 1D deviation profiles. This approach was later extended by Colosimo et al. [8], who introduced two innovations: (i) a weighted modeling scheme to account for layerwise variability in image reconstruction, and (ii) a control-charting framework for automatic detection of anomalous deviations affecting one or multiple unit cells.

While these methods show strong potential for industrial application, several challenges still hinder their readiness for deployment. First, achieving accurate and repeatable image segmentation under real production conditions remains difficult, yet it is essential for reliable geometry reconstruction. Second, the selection of appropriate deviation metrics is critical to ensuring effective defect detection while limiting data storage and computational overhead. Finally, although previous studies demonstrated the feasibility of low-dimensional monitoring approaches for lattice structures, validation has so far been restricted to limited experimental scenarios in which only simulated deviations were considered.

Ensuring that in-situ monitoring methods remain insensitive to environmental and operating conditions (e.g., chamber illumination) and to part-to-part or layer-to-layer variations in size and geometry is fundamental for achieving reliable and repeatable performance in industrial settings. However, if not carefully tuned, powder-bed image segmentation may lack sufficient accuracy and consistency of geometry reconstruction [9]. The present work inherits and extends seminal studies by addressing the industrial gaps mentioned above. More specifically, we investigate a low-dimensional deviation detection approach suitable to be used in-situ and in-process taking advantage of industrial in-situ sensing setups. To this aim, we address a class of segmentation approaches based on active contours, with a particular emphasis on calibration aspects that have received limited attention in the existing literature. Building on this analysis, we propose practical guidelines for industrial implementation, aimed at supporting the effective adoption of in-situ monitoring and inspection practices.

The major contributions with respect to the previous literature are the following: 1) first, the study investigates the critical role played by image segmentation calibration to enhance the in-situ geometry reconstruction accuracy, showing that robustness to variations in the illumination settings and/or part size and geometrical features could be achieved; 2) it investigates and compare deviation metrics aiming to enhance the detection of actual anomalies and defects and providing guidelines for practitioners; 3) it evaluates the performance of the method in the presence of real geometrical deviations occurred during the L-PBF of lattice structures.

A real case study involving the production of metal gyroid lattice structures is presented. Structures having different wall thickness were manufactured via L-PBF. They were inspected in-situ via post-exposure powder bed imaging, whereas ex-situ inspection via X-ray CT was used as ground truth. The analysis addressed both part-to-part and build-to-build variability sources and their effects on the in-situ geometry reconstruction accuracy. Controlled defect induction finally allowed us to test and verify the performance of the proposed approach as well as highlighting limits and possible research directions for further improvements.

The paper is organized as follows. Section 2 presents the materials and methods. Section 3 presents the performances and results achieved in the real case study. Section 4 presents a discussion about strengths and open challenges that characterize the proposed methodology. Section 5 concludes the paper.

2. Materials and methods

2.1. Experimental settings

Copies of gyroid lattice structures with different geometrical properties were manufactured via L-PBF using a 3D-NT LLA150 system by Prima Additive featuring a fiber laser source (AFX-1000, nLIGHT). The gyroid structures were manufactured in AlSi10Mg with a powder size distribution in the range 15–50 μm (D10 – D90). Two builds were performed, each consisting of 4 structures of size 40 × 40 x 40 mm. In each build, two copies were manufactured with a wall thickness of 0.8 mm (thin wall), and two copies with a wall thickness of 2 mm (thick wall). The unit cell size was 10 × 10 x 10 mm, thus every structure consisted of 4 × 4×4 unit cells. Fig. 1 shows the nominal shape of the two structures.

Fixed process parameters were applied for all the gyroid structures in both builds. The selection of process parameters was based on previous optimization studies for AlSi10Mg parts on the same 3D-NT LLA150 system. They are summarized in Table 1.

Lattice structures were manufactured using a single-track exposure strategy without contour scans, as commonly adopted for thin strut geometries in L-PBF, where the feature size is comparable to the melt pool width. A single set of process parameters was intentionally used for both thin and thick features to ensure a controlled comparison and to assess the robustness of the proposed method under uniform processing conditions, avoiding geometry-specific tuning of process parameters.

The L-PBF system was equipped with an industrial IDS UI-5490SE-M-GL powder bed camera, featuring a 10.55 Mpix sensor, which enabled a spatial resolution of about 57 μm/pixel within a field of view that embraced the whole build area. The camera was installed as shown in Fig. 2, exploiting one of the two available viewports on the ceiling of the build chamber. The viewing angle can inflate artifacts and distortions in the powder bed image after the perspective correction operation is applied. The sensitivity of rectified images to such perspective effects can be quantified by the aspect ratio distortion introduced by the projective mapping [17]. In first approximation, for a planar surface viewed at angle θ from the normal, the compression along the viewing direction scales with $\cos\theta$. As a result, the corresponding stretch needed during image rectification scales approximately with $1/\cos\theta$. The distortion is null at $\theta = 0^\circ$ and remains below 20% for $\theta \leq 35^\circ$, then it quickly inflates and it doubles $\theta = 60^\circ$. Using the viewport available on the 3D-NT LLA150 system, the viewing angle was about $\theta = 25^\circ$, for which the induced distortion is expected to have a limited impact on the segmentation accuracy and the reconstruction of geometrical features.

The camera installation and optical settings were the same in both builds, but the lighting setup was varied from build to build. The purpose was to investigate the influence of environmental conditions (the powder lighting being the most important one) on the in-situ geometry reconstruction accuracy, highlighting the need for proper segmentation tuning and calibration.

In build 1, a dark field condition [20] was generated by placing a directional light source beside the powder bed camera, exploiting the second viewport on the ceiling of the build chamber. Dark field is known to be a beneficial lighting condition for image segmentation, while it is less effective for other purposes, like surface texture characterization. In build 2, a more traditional lighting configuration was applied, involving multiple LED stripes inside the build chamber, mounted on the ceiling. This second setup enables a more diffused light on the powder bed, possibly emphasizing local contrasts and surface irregularities, but not optimal for image segmentation. For a discussion on the illumination role on powder bed image quality, the reader is referred to Caltanissetta et al. [7].

The same layout was applied in both builds in terms of gyroid structure placement, with thin wall structures in location 1 and 4, and thick wall structures in location 2 and 3 (see Fig. 2). Build 1 was performed without induced defects and used as representative of the natural process variability in the presence of good quality parts. During

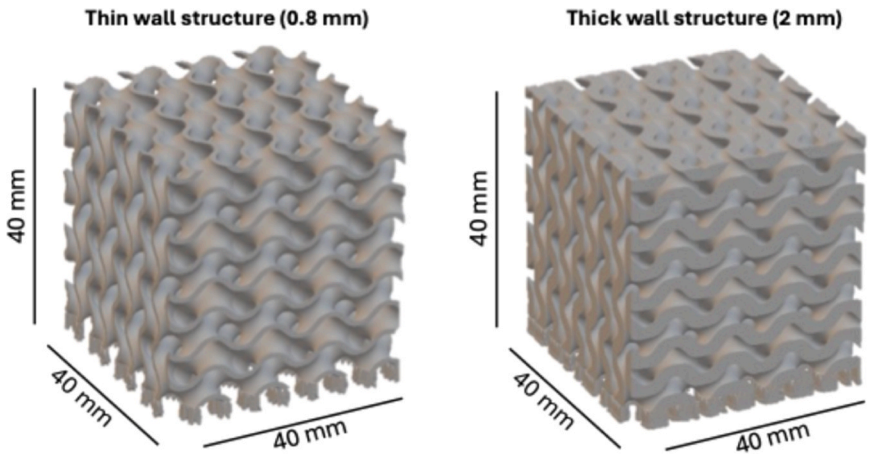

Fig. 1. – Thin wall (left) and thick wall (right) gyroid lattice structures used in the study.

Table 1 –
L-PBF process parameters.

Layer thickness	Power	Scan speed	Hatch distance	Hatch rotation	Contours
0.03 mm	320 W	1200 mm/s	0.15 mm	67°	none

build 2, instead, geometrical deviations were induced by using a damaged recoating system. The rubber blade of the recoater was damaged by applying two indentations by means of a cutter. Specifically, as shown in Fig. 2, two different indentations were produced: one with high severity (4 mm wide and 1 mm deep) and one with low severity (1 mm wide and 1 mm deep). They were introduced in two different locations of the build, such that structures in location 1 and 2 of build 2 were affected by the high severity one, and structures in location 3 and 4 of the same build were affected by the low severity one. The high severity indentation produced a visible anomaly in the powder bed image with an average width of about 0.8 mm, equal to the smallest wall thickness of manufactured structures. The low severity one produced a visible anomaly with average width of about 0.4 mm. Such widths are respectively 14 times and 7 times larger than the spatial resolution of the camera.

At the end of the process, all parts were inspected via X-ray CT using a Phoenix v|tome|x m 350 kV system, with a voxel size of 40 μm. Such resolution was constrained by a field of view sufficiently large to include the whole lattice structure.

Despite the intrinsic limitations of X-ray CT as a ground truth reference for AM parts, which include segmentation uncertainty and resolution-dependent effects as highlighted in Du Plessis et al. [12], it remains the only viable technique for non-destructive 3D characterization of complex shapes like lattice structures. In the present study, X-ray CT data were used exclusively during the active contour calibration phase. Specifically, CT-based ground truth was employed to compare the relative performance of different segmentation parameter sets, rather than to provide absolute geometrical measurements. In this context, the most critical requirement is the consistency of the CT data across all samples used in the calibration process. The segmentation of the CT data was performed using a standard histogram-based thresholding approach implemented in VGStudio MAX (Volume Graphics GmbH). The threshold value was selected based on the bimodal distribution of voxel intensities and applied as consistently as possible across all samples acquired under the same CT-scanning conditions.

Following thresholding, the segmented volumes were exported in STL format and aligned to the nominal geometry using the Iterative Closest Point (ICP) algorithm implemented in MeshLab. The aligned CT data were finally sliced to generate binary ground truth masks for every manufactured layer.

2.2. *In-situ geometry reconstruction*

Inheriting the modelling framework introduced in Colosimo et al. [8], a lattice structure can be represented by an array of N unit cells of fixed shape and size, placed side by side in a regular grid along the x and y directions, and stacked on top of one another along the z direction. Using this notation, z coincides with the build direction. We also assume all unit cells have the same bounding box dimensions, and they consist of the same number of layers. Generalizing the method to geometries

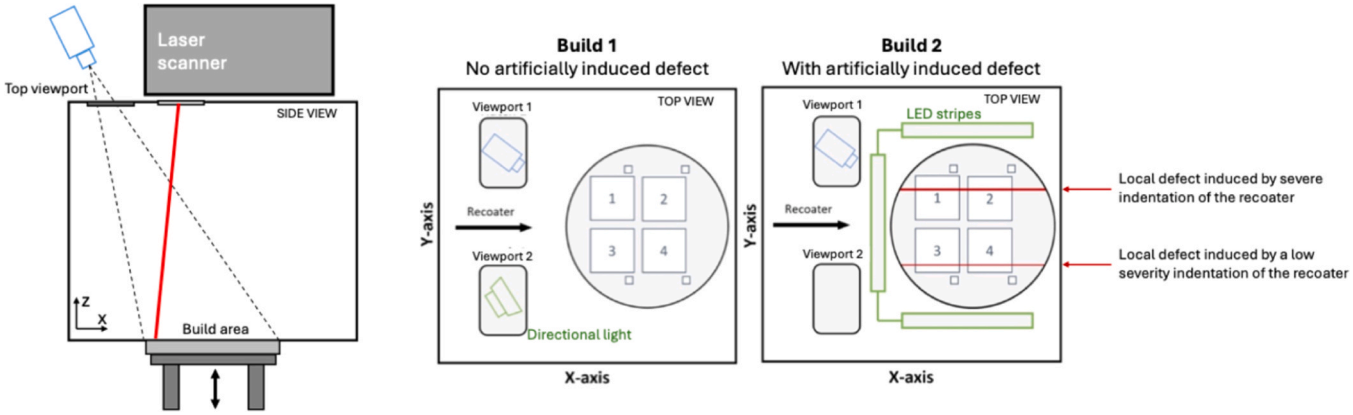

Fig. 2. – Powder bed imaging and lighting setup used in the two builds.

that do not comply with this assumption represents an on-going development of the proposed approach.

In-situ geometry reconstruction begins with a pre-processing step that corrects the perspective of the powder bed image and aligns it with respect to the nominal shape gathered by slicing the originating STL file. In this study, a standard landmark-based projective alignment algorithm was applied [30], but a comprehensive view on these methods can be found in Szeliski [30] and Avants et al. [4]. Image segmentation is then applied to identify the contours of the solidified layer in post-exposure powder bed images. To this aim, we adopted the "active contours" method [23,27,29].

The algorithm iteratively refines an initial boundary, i.e., the nominal geometry of the current layer, by applying shrink/expand operations guided by the minimization of an energy functional, implemented via a level set approach [26]. This method has been increasingly adopted in the L-PBF literature due to its effectiveness in dealing with powder bed images leveraging on known nominal geometries as initial boundary [8,28], 2022, [1,7,22,27].

Several variants of the active contour methodology have been developed so far. So-called region-based approaches rely on pixel intensity differences inside and outside the detected contour, whereas edge-based ones focus on the gradients of pixel intensities to identify the boundary that separates the foreground from the background. Each method has its own benefits and drawbacks. Region-based approaches may provide better performances in the presence of images having a good contrast but weak edges and smooth transitions between foreground and background. Conversely, edge-based approaches may provide better performances when different regions exhibit poor differences of average pixel intensities but abrupt local transitions along the boundary.

In this study, we refer to the method advocated in Pagani et al. [27], where edge- and region-based methods were combined in a unified formulation. Let Ω be the region of the image that corresponds to the foreground, i.e., the solidified layer, and $\delta\Omega$ be its contour. Let also $d(x, \delta\Omega)$ be the distance between any pixel x and the contour $\delta\Omega$, estimated by means of a 2-D Euclidean distance transform [13]. By defining a signed distance $\varphi(x)$ defined as:

$$\varphi(x) = \begin{cases} -d(x, \delta\Omega) \text{ if } x \in \Omega \\ d(x, \delta\Omega) \text{ if } x \notin \Omega \end{cases} \quad (1)$$

the identified contour at iteration t is the zero level set of such distance function. By combining the region- and edge-based methods, the signed distance evolves as follows:

$$\frac{\delta\varphi(x,t)}{\delta t} = w\theta_{region} + (1-w)\theta_{edge} \quad (2)$$

where θ_{region} and θ_{edge} are the region and edge terms of the algorithm, respectively, and w is a weight to balance the influence of these two terms in the convergence to the final reconstructed contour. The weight w is such that $0 \leq w \leq 1$, where $w = 0$ corresponds to a purely edge-based segmentation, whereas $w = 1$ to a purely region-based one. Additional details about the active contour formulation can be found in Pagani et al. [27].

The weight w is just one of several parameters that should be selected and tuned to maximize the in-situ reconstruction accuracy. Other parameters included in the active contour implementation adopted in this study are listed in Table 2, together with their reference values.

The number of iterations shall be set large enough to guarantee the convergence of the iterative segmentation. In this study, 30 iterations resulted to be sufficient, since the reconstructed geometry was quite close to the initial (nominal) one. The parameter r_{kernel} is the radius of the kernel used for local spatial weighting around the evolving contour. In this study, a dense stencil of width $1+2r_{kernel}$ was used. The kernel is essentially associated to the region-based term, since the edge-based term exploits a global gradient function. The parameters α_{sig} and β_{sig} are two parameters of the sigmoid function that determines the rate and direction at which the contour evolves along the successive iterations. Setting $\alpha_{sig} = -3$ and $\beta_{sig} = 0$ is a common choice: the former allows slowing down the contour evolution in the presence of features with higher pixel intensity variability, while the latter means that no a-priori target is defined on the gradient magnitude that activates the contour evolution. Eventually, the "balloon" parameter acts as a sort of directional penalization, such that a positive value forces the contour to expand outward, while a negative value forces it to shrink inward. Setting a zero value (like in this study) imposes no such directional preference. Setting a balloon value greater or lower than zero is helpful if one knows that the boundary of the foreground region is either entirely outside or inside the nominal contour.

Table 2 –
Active contour parameters and reference values.

Parameter	# iterations	r_{kernel}	w	α_{sig}	β_{sig}	Balloon
Value	30	Subject to calibration	Subject to calibration	-3	0	0

In principle, all parameters should be tuned for the specific application. In the mainstream literature, however, limited or no attention is devoted to the optimal choice of their values, and there is a lack of studies on their influence on the image segmentation performance. In this study, we focused our analysis to parameters w and r_{kernel}, as they are known to have a major impact on the segmentation performance. The calibration procedure for the selection of these parameters is described in sub-Section 2.3, whereas additional guidelines are discussed in Section 4.

2.3. In-situ estimation and monitoring of shape deviations

The image segmentation produces a binary image, where the pixels in the foreground (solidified layer) regions represent a connect component of area $\widehat{A}$. Comparing this region with the nominal shape of layer, it is possible to determine to what extent the in-situ reconstructed geometry deviates from the nominal.

Different deviation metrics can be used to this aim. Colosimo et al. [8] used the difference between the in-situ reconstructed area, $\widehat{A}(z)$, and the nominal area, $A_{NOM}(z)$, in the z-th layer as synthetic descriptor:

$$\delta_{Area}(z) = \widehat{A}(z) - A_{NOM}(z) \quad , \quad z = 1, 2, \ldots \quad (3)$$

Other possible metrics rely on the intersection between the in-situ reconstructed region and the nominal one, as shown in Fig. 3.

In this study we introduce another deviation metric, namely the area of the discrepancy between the two regions, defined as follows:

$$D_{tot}(z) = [A_{NOM}(z) \cup \widehat{A}(z)] - [A_{NOM}(z) \cap \widehat{A}(z)], \quad z = 1, 2, \ldots \quad (4)$$

The deviation metric $D_{tot}(z)$ is also referred to as "symmetric difference" or "disagreement area" [21]. Differently from similarity metrics commonly used in machine vision, as Intersection over Union (IoU) or the Dice similarity coefficient, $\delta_{Area}(z)$ and $D_{tot}(z)$ provide a direct quantification of the extent or severity of the deviation in physical terms (e.g., number of pixels converted into a measurable area).

By subtracting the intersection between the two areas from their union, the $D_{tot}(z)$ metric quantifies the discrepancy between them. It is worth noticing that $D_{tot}(z)$ does not coincide with the difference of the areas, $\delta_{Area}(z)$. Consider the extreme case where the $A_{NOM}(z) = \widehat{A}(z)$, but they are not overlapped, thus $A_{NOM}(z) \cap \widehat{A}(z) = 0$. In this case, $\delta_{Area}(z) = 0$ while $D_{tot}(z) = A_{NOM}(z) + \widehat{A}(z)$.

$D_{tot}(z)$ shares conceptual similarities with other overlap-based distance measures that saturate once the two regions no longer intersect [21]. Since the objective is primarily to quantify geometric deviations in

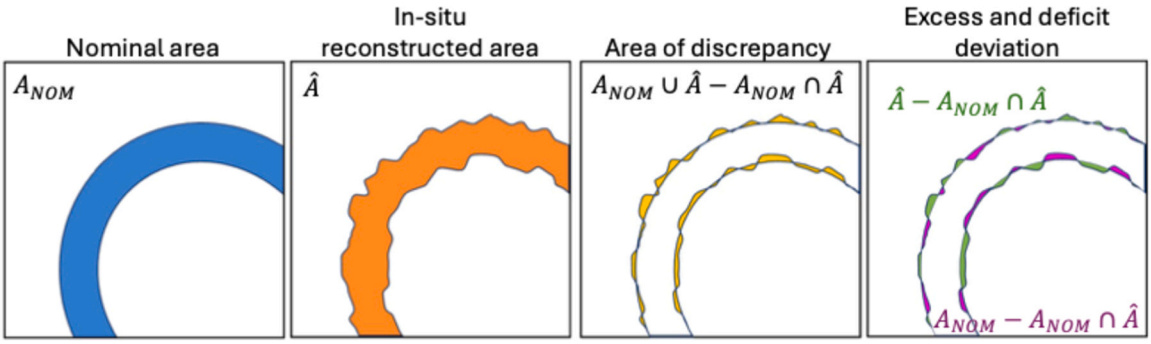

Fig. 3. – Example of how different deviation metrics are estimated.

terms of mismatch between the nominal and reconstructed cross-sectional areas, saturation indicates a complete lack of overlap with respect to the nominal geometry. However, it is possible to extend the metric to incorporate spatial separation between disjoint regions. A more in-depth discussion on the selection of deviation metrics and their possible alternatives is provided in Section 4.

Generally speaking, $D_{tot}(z)$ allows quantifying deviations from the nominal that can be caused by a variation in size, shape and/or translation of the in-situ reconstructed shape. On the contrary, $\delta_{Area}(z)$ allows quantifying a variation in size, being insensitive to where the in-situ reconstructed region spatially locates with respect to the nominal one. Thus:

- $D_{tot}(z)$ is more sensitive to any possible deviations that affect the overlap between the in-situ reconstructed region and the nominal, but this makes it also more sensitive to possible alignment errors between the two regions;
- $\delta_{Area}(z)$ only depends on the area of the two regions, regardless of their relative location in space and their actual overlap, but it is more robust to possible alignment errors.

As regards misalignment errors between the nominal and reconstructed regions, they result in an overestimation of the deviation and may cause higher false positive rates. This is particularly critical for thin features like the ones of lattice structures. This effect can be mitigated during the camera calibration stage, by ensuring the registration between in-situ images and the nominal geometry to be as accurate as possible. However, residual misalignment errors may still arise from several sources, including lens distortions, imperfect perspective correction, drifts in the camera mounting setup, etc. Misalignment errors can be quantified with the aid of human supervision during the calibration phase. If residual errors are in an order of magnitude that is not negligible with respect to the severity of anomalies to be detected in-situ, using a region-based (rather than point-wise) metric like $\delta_{Area}(z)$, which is insensitive to misalignment errors, may be recommended. For a further discussion on the selection of deviation metrics, the reader is referred to Section 4.

The deviation metric $D_{tot}(z)$ can also be decomposed into two "directional" terms, one capturing the overall excess of material with respect to the nominal, and one capturing the overall deficit (or lack) of material:

$$D_{tot}(z) = D_{excess}(z) + D_{deficit}(z), \quad z = 1, 2, \ldots \tag{5}$$

A simple example to clarify the differences among these metrics in shown in Fig. 3.

Eq. (3) and Eq. (4) are useful to express the deviation in absolute terms. This makes them particularly suitable for industrial applications, where the ultimate goal is not only to assess algorithmic accuracy in relative terms, but also to estimate the practical significance of detected deviations with respect to part quality requirements. However, for the purpose of performance comparison in the presence of lattice structures having different exposed areas, all computed deviations were normalized with respect to the nominal area. Moreover, deviations were computed for each individual unit cell of the structure, leading to the following expressions:

$$\delta_{Area\,i}(z) = 100 \times \frac{\widehat{A_i}(z) - A_{NOMi}(z)}{A_{NOMi}(z)}, i = 1, \ldots, N, \quad z = 1, 2, \ldots$$

$$D_{tot\,i}(z) = \frac{100 \times [A_{NOMi}(z) \cup \widehat{A_i}(z)] - [A_{NOMi}(z) \cap \widehat{A_i}(z)]}{A_{NOMi}(z)}, \quad i = 1, \ldots, N, \quad z = 1, 2, \ldots \tag{6}$$

Following the route presented in Colosimo et al. [8], the 1-D pattern of the deviation estimated in-situ for the i-th unit cell along the build direction, z, can be used as a synthetic "signature" of the dimensional and geometrical consistency of the unit cell itself. This aids the detection of local distortions affecting one or more unit cells, especially if such distortions are persistent across multiple layers. The 1-D modelling and monitoring scheme proposed in Colosimo et al. [8] has been used and tested in this study. The salient steps are described hereafter, but for full details we refer the reader to Colosimo et al. [8].

Once a complete layer of cells has been printed, the 1-D profile of the deviation from the nominal, $\Delta_i(z)$, can be estimated for each unit cell, where Δ_i is a generic notation, which can be replaced by any specific deviation metrics described above, e.g., $\Delta_i(z) = \delta_{Area\,i}(z)$, or $\Delta_i(z) = D_{tot\,i}(z)$.

A weighted least square (WLS) B-spline model can be used to fit the deviation profiles, to enhance the anomaly detection performance. The model can be formulated as:

$$\widehat{\Delta}_i(z) = \sum_{q=1}^{Q+L-1} B_q(z, \tau) P_{i,q} \quad , \quad i = 1, \ldots, N, \quad z = 1, 2, \ldots \tag{7}$$

where B_q are the B-Spline basis functions of order Q (in this study, $Q = 3$), and $\boldsymbol{\tau} = \{\tau_l, l = 1, 2, \ldots, L-1\}$ is the knot sequence where L is the number of subintervals. $P_{i,j,h,1}, P_{i,j,h,2}, \ldots, P_{i,j,h,Q+L-1}$ are the control points for the i-th unit cell computed as follows:

$$P_i = \left(B^T W(z) B\right)^{-1} B^T W(z) A_i(z), \quad i = 1, \ldots, N \tag{8}$$

where B is the model matrix of B-splines basis functions and $W(z)$ is a diagonal matrix whose diagonal elements are the weights $\omega(z)$. The rationale behind this weighting matrix consists of relying on intrinsic image properties in every layer to enhance the fitting, giving lower weight to layers where the properties of the image account for a higher reconstruction uncertainty, and higher weight to other layers. The weight $\omega(z)$ can be estimated as the inverse of the pixel intensity variance around the nominal contour in the z-th layer:

$$\omega(z) = \frac{1}{{s_b}^2(z)} \quad , \quad z = 1, 2, \ldots \tag{9}$$

where ${s_b}^2(z)$ is the pixel intensity variance within a band region centered on the nominal contour, which extends n_b pixels inward and n_b pixels outward (in this study, $n_b = 3$).

Fitted profiles $\widehat{\Delta}_i(z)$ can then be used to design a control charting scheme suitable to automatically detect deviation patterns affecting one or more unit cells. This methodology entails two sequential phases, namely a design (or calibration) phase and a use phase.

A more general scheme than the one presented in Colosimo et al. [8] is introduced here, which also takes into consideration the tuning of the image segmentation parameters. The methodology can be schematically summarized as follows:

- **Calibration phase**

  - Production of M copies of the same part (or simple test specimens whose geometry is representative of specific geometrical features of interest), with the processing and imaging conditions that will be adopted in the use phase.
  - In-situ powder bed image collection during the L-PBF process.
  - X-ray CT scan of the M copies in their as-printed state after the L-PBF process, to be used as ground truth; slicing of the CT reconstruction and alignment of the ground truth geometry to the nominal geometry in every layer of the build.
  - Choice of the deviation metric, $\Delta_i(z)$ (e.g., $\Delta_i(z) = \delta_{Area i}(z)$, or $\Delta_i(z) = D_{tot i}(z)$). Guidelines for this choice are provided in the following.
  - Estimation of deviation profiles $\widehat{\Delta}_i(z)$ between the in-situ reconstruction and the ground truth geometry, by varying the active contour parameters within a predefined range.
  - Selection of the set of active contour parameters that minimize the average deviation from the ground truth. Let's refer to the deviation estimated with tuned parameters as $\widehat{\Delta}_i^{GT}(z)$, where GT strands for "ground truth", to differentiate it from the deviation from the nominal to be estimated in the use phase. For each unit cell of lattice structures used in the calibration phase, the root mean square (RMS) of the weighted b-splines fitted on profiles of deviation from the ground truth, $RMS\left(\widehat{\Delta}_i^{GT}(z)\right)$, is computed. Then, the average RMS value for all unit cells of all calibration samples can be used as objective function to be minimized. Thus, the objective function is computed by aggregating all deviations from the ground truth pooled across all z-coordinates and samples in the calibration build. Optimal values can be searched with a grid exploration of parameters w and r_{kernel} in predefined ranges. More efficient optimization methods could be possibly used, to reduce the computational effort with respect to a full grid search. The same objective function and the same procedure can be applied regardless of the specific deviation metric, either $\delta_{Area}(z)$ or $D_{tot}(z)$, selected to determine $\widehat{\Delta}_i^{GT}(z)$.
  - Estimation of the standard error of the deviation $\widehat{\Delta}_i^{GT}(z)$ for each copy of the lattice structure, $s_{\Delta,1}, \ldots, s_{\Delta,k}, \ldots, s_{\Delta,M}$.
  - Estimation of the overall pooled standard deviation, $s_\Delta = \frac{1}{M}\sum_{j=1}^{M} s_{\Delta,j}$, as a measure of the natural variability of the deviation from the ground truth.
  - The control limits used for anomaly detection are estimated from the calibration data, which represent defect-free conditions. Specifically, we compute the average deviation from the ground truth, denoted as $\overline{\widehat{\Delta}}(z)$ and its corresponding standard deviation s_Δ, which captures the natural variability of the deviation in the absence of defects. The upper and lower control limits (UCL and LCL) are then defined as:

$$[UCL, \quad LCL] = \overline{\widehat{\Delta}}(z) \pm k s_\Delta,$$

where the coefficient k determines how far the limits are placed from the average value (larger values of k lead to wider control limits and therefore fewer false alarms, while smaller values increase sensitivity to deviations). As done in common statistical process monitoring practices, k is selected based on a target false positive rate (also known as Type I error), assuming a normal distribution of the deviation under defect-free conditions. Specifically, $k = z_{\alpha/2}$, where $z_{\alpha/2}$ is the upper $100\left(\frac{\alpha}{2}\right)\%$ percentile of the standard normal distribution corresponding to a desired false alarm probability α. Since multiple layers are monitored within each unit cell, the overall (family-wise) false positive rate is controlled by adjusting the per-layer error probability as $\alpha^* = \alpha/l$, where l is the number of layers and α is the target false alarm probability, e.g., $\alpha = 0.0027$, which is a common choice used in statistical process control, Montgomery [25]. This ensures that the probability of generating at least one false alarm within a unit cell remains equal to the desired target level.

- **Use phase**

  - For each i-th unit cell of every new manufactured lattice structure, the 1-D deviation from the nominal, $\widehat{\Delta}_i(z)$, is estimated, using the same deviation metric adopted during the calibration phase, as well as the tuned active contour parameters identified during the calibration phase.
  - Compare the current deviation profile, $\widehat{\Delta}_i(z)$, with the control limits estimated in the calibration phase, *UCL* and *LCL*, and signal an alarm if a violation of the limits is present in at least p consecutive layers, where $p \geq 1$.
  - Repeat the previous two steps for every unit cell of every new manufactured lattice structure.
  - Notice that no re-calibration is needed unless any major source of variability from build-to-build or part-to-part has been introduced (e.g., a change of material, process parameters, monitoring equipment, etc.). In case of systematic location effects, or other known part-to-part variations, the control chart parameters, $\overline{\widehat{\Delta}}(z)$ and s_Δ, can be adapted accordingly. As an example, if the pattern of deviation profiles is affected by the part location within the build area, e.g., because of light inhomogeneity, $\overline{\widehat{\Delta}}(z)$ and s_Δ can be replaced by their location-dependent counterparts, thus adapting to natural sources of variability.

3. Results

An example of raw and aligned powder bed images acquired during the production of the test specimens is shown in Fig. 4. Fig. 4 (right panel) also shows the as-built structures in build 1.

The experimental results are presented in the following sub-sections. Sub-Section 3.1 presents the tuning of active contour parameters and their influence on the in-situ reconstruction accuracy. Sub-Section 3.2 presents the in-situ defect detection performance and the role played by the choice of the deviation metric.

3.1. Active contour tuning

Two gyroid structures manufactured in build 1, one with wall thickness of 0.8 mm and one with wall thickness of 2 mm, were used to tune the active contour parameters, w and r_{kernel}. Optimal values were searched with a full grid exploration of parameters in the ranges $0 \leq w \leq 1$ and $1 \leq r_{kernel} \leq 12$ (expressed in number of pixels), with a step of 0.05 for w and a step of 1 for r_{kernel}. Regarding parameter w, values 0 and 1 represent the extreme conditions, namely purely edge-based ($w = 0$) and purely region-based ($w = 1$) segmentation. Regarding parameter r_{kernel}, the selected range was deemed appropriate to explore a wide range of kernel radii, up to 12 times the spatial resolution of the camera.

The same procedure was repeated in build 2. Indeed, different

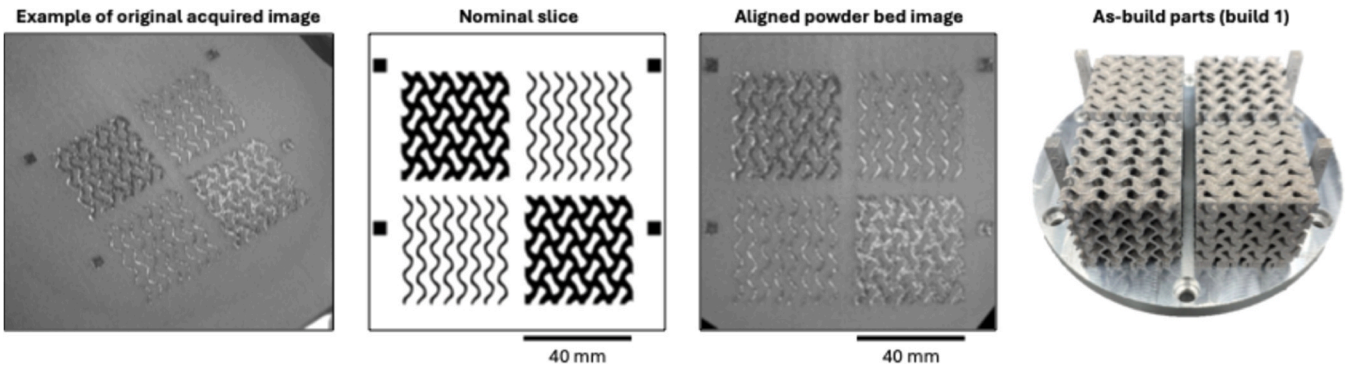

Fig. 4. – Example of powder bed images before and after the perspective correction and alignment to the nominal geometry; as-build parts in build 1 are shown on the right.

lighting settings were used in the two builds. Thus, repeating the calibration in build 2 was aimed to determine the sensitivity of active contour segmentation on build-to-build variations caused by the different illumination. It is worth noticing that in build 2 some cells were affected by the defect injected by damaging the recoater, and hence only the unit cells in locations not affected by such damage were used to tune the active contour parameters.

Fig. 5 shows the output of the calibration in terms of the average RMS deviation from the ground truth in the two builds as a function of controlled parameters. The analysis refers to the use of the $\delta_{Area}(z)$ metric. Similar results were observed for the $D_{tot}(z)$ metric (additional details and full results for both the deviation metrics are presented in the following).

The condition $w = 0.5$ and $r_{kernel} = 5$ was used as a starting reference, as it was used in previous studies [27], and it involves an equal weight associated to edge and region terms of the active contour algorithm.

In both builds, the minimum RMS of the deviation was achieved for $w = 0$, namely by using a purely edge-based active contour segmentation. For $w = 0$, the parameter r_{kernel} has no influence, as it employed only in the region-based term. Reducing the weight w, the optimal value of r_{kernel} reduces too, but its influence tends to vanish as w approaches 0.

The relative improvement with respect to the reference setting ($w = 0.5$ and $r_{kernel} = 5$) is higher in build 2 than in build 1, but, most importantly, the optimal choice of the active contour parameters is the same in both builds.

This testifies that the in-situ contour reconstruction can be made robust to build-to-build variations in the illumination conditions, which is known to be a primary source of data variability in machine vision. It also highlights the importance of a calibration procedure to estimate the optimal tuning parameters to segment powder bed images.

Fig. 6 shows an example of purely edge-based ($w = 0$) active contour segmentation of two sample layers in build 1. Fig. 7 shows an example of 1-D profiles of deviations from the ground truth estimated for unit cells with different wall thickness. In this example, the $\delta_{Area}(z)$ deviation metric was used. Fig. 7 shows the raw deviation profiles, the WLS fitted profiles and the residuals. It is interesting to note that such deviation profiles oscillate around the 0 value, which indicates the absence of biases with respect to the ground truth. Moreover, the fitted profiles, $\widehat{\delta}_{Area}(z)$, allow getting rid of the layer-by-layer variability while capturing the underlying systematic pattern that is mainly driven by the lattice geometry itself.

A quantitative comparison on the influence of optimal tuning parameters on the in-situ reconstruction accuracy and robustness to varying conditions is summarized in Fig. 8 and Fig. 9. Two sets of compared active contour parameters are referred to as "ref" ($w = 0.5$ and $r_{kernel} = 5$), "edge" (purely edge-based, $w = 0$), respectively.

The analysis refers to a validation set including only gyroid cells of structures not included into the previous calibration. Again, in build 2, only cells not affected by the injected defects were considered. Results were compared in terms of 1) the RMS deviation from the ground truth and 2) the prediction variance, $V[\widehat{\delta}_{Area}(z)]$ or $V[\widehat{D}_{tot}(z)]$.

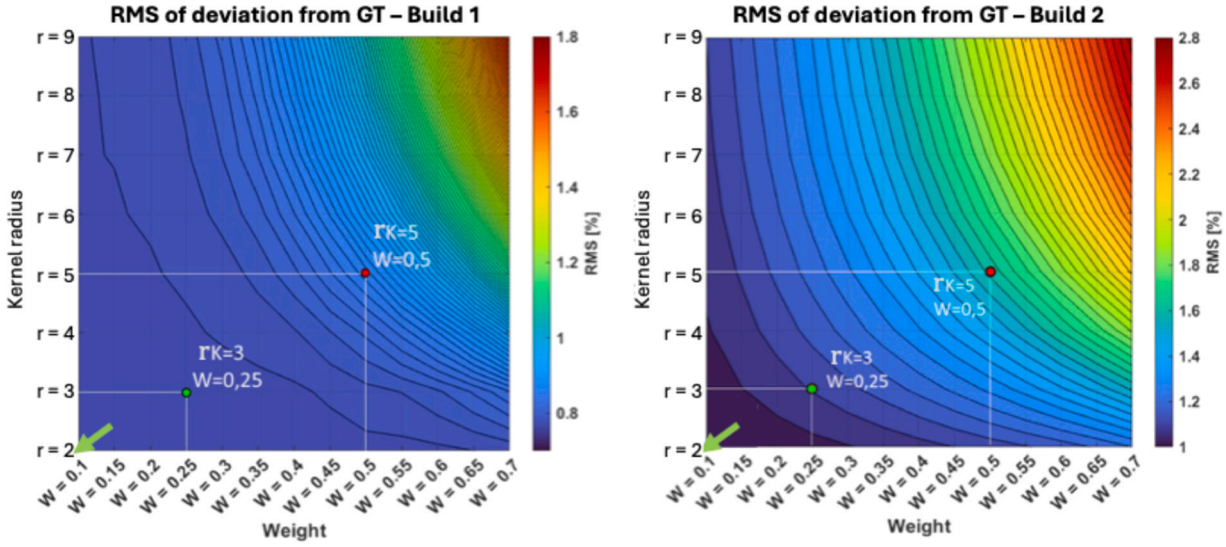

Fig. 5. – Average RMS of the deviation from the ground truth in build 1 (left) and build 2 (right) depending on the two controlled parameters, i.e., the weight that balances the edge- and region-based terms, and the kernel radius.

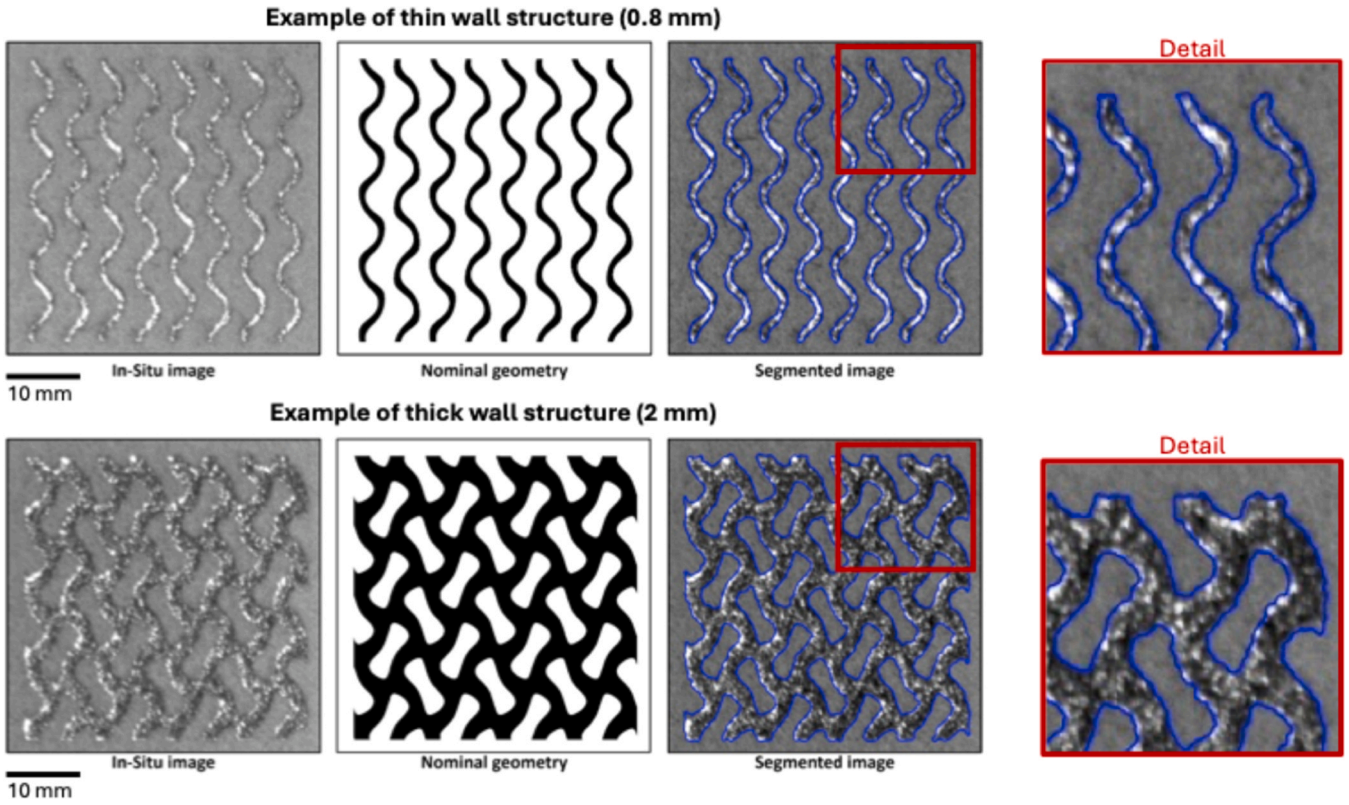

Fig. 6. – Examples of in-situ reconstruction of a thin wall (top) and thick wall (bottom) structure using the purely edge-based active contour.

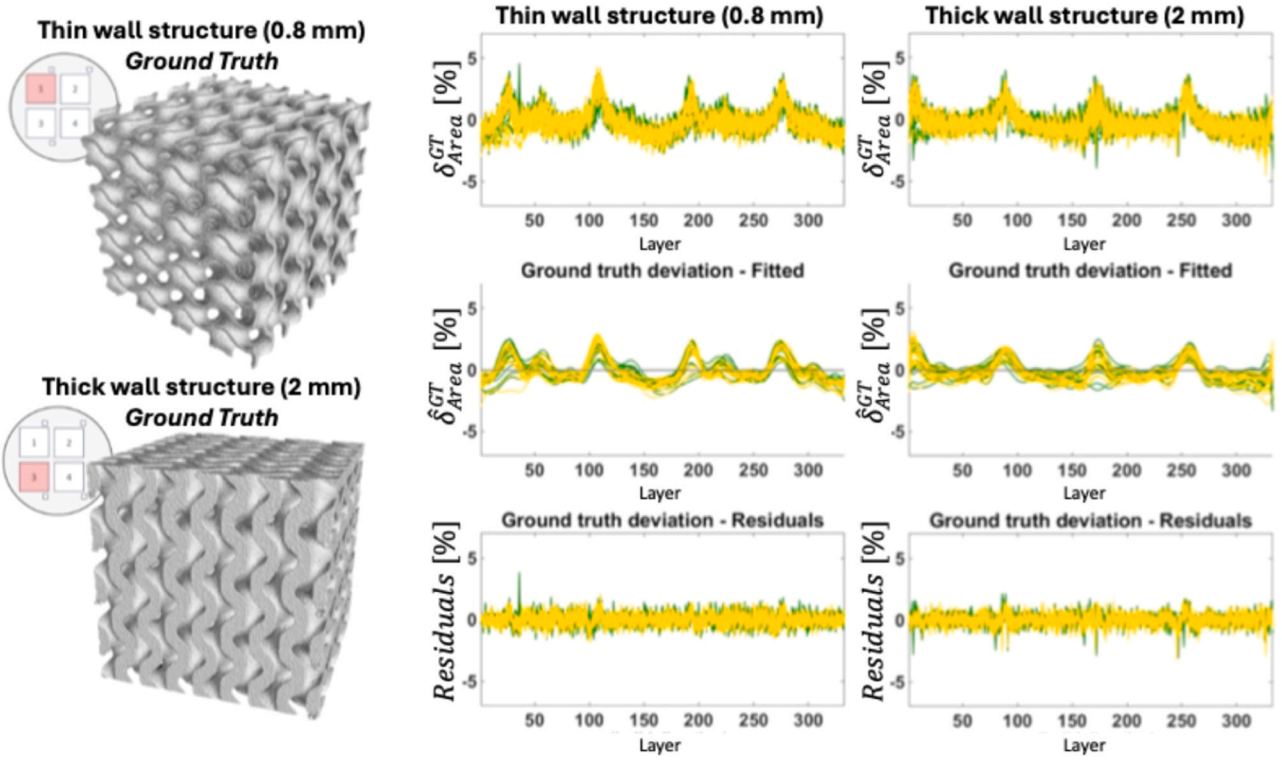

Fig. 7. – Left panel: X-ray CT reconstruction of thin and thick wall structures used ad ground truth; right panel: examples of raw deviation profiles from the ground truth using the $\delta_{Area}(z)$ metric, the corresponding WLS fitting and residuals (different colors indicate unit cells belonging to different samples).

Fig. 8 shows the 95% confidence intervals for the effect of the different illumination settings and the different lattice wall thickness on the mean RMS of the deviation from the ground truth and its prediction variance using the $\delta_{Area}(z)$ deviation. Fig. 9 shows the 95% confidence intervals for the effect of the different illumination settings and the different lattice wall thickness on the mean RMS of the deviation from

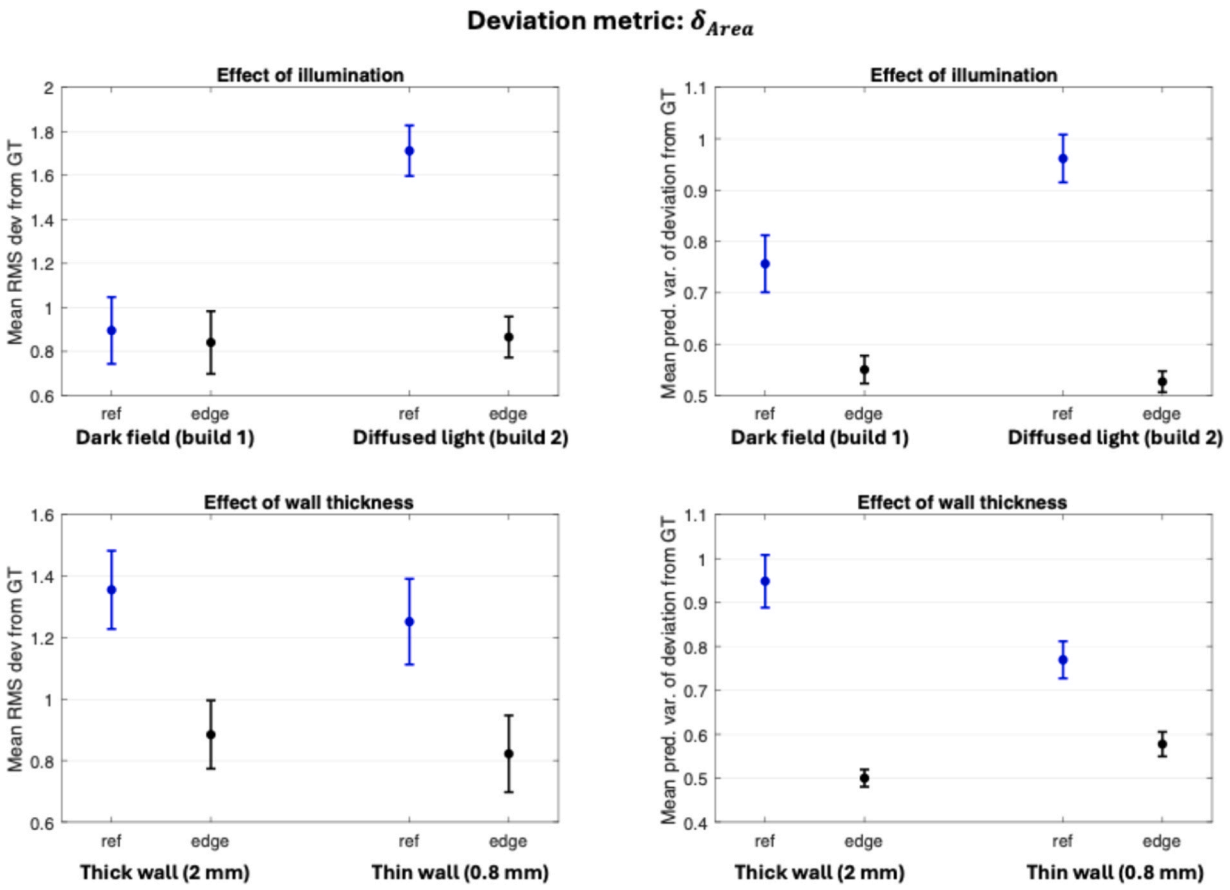

Fig. 8. – 95% confidence intervals for the effect of the different illumination settings and the different lattice wall thickness on the mean RMS and the prediction variance using the $\delta_{Area}(z)$ deviation for different choices of the active contour parameters (ref, edge).

the ground truth and its prediction variance using the $D_{tot}(z)$ deviation.

The salient outcomes of Fig. 8 and Fig. 9 can be summarized as follows:

- The edge-based active contour segmentation yields a statistically significant improvement of the in-situ geometry reconstruction accuracy with respect to the reference condition, both in terms of RMS of the deviation from the ground truth and the mean prediction variance of the deviation.
- The improvement is more significant when considering the $\delta_{Area}(z)$ deviation.
- The change of illumination settings from build 1 to build 2 had no statistically significant effect on the in-situ reconstruction accuracy enabled by the purely edge-based active contour segmentation. This highlights that the edge-based method made the segmentation insensitive to a variation from dark field to diffused light, leading to more robust results.
- Similarly, the wall thickness variation from 2 mm to 0.8 mm had no statistically significant effect on the in-situ reconstruction accuracy enabled by the purely edge-based active contour segmentation. This highlights that the edge-based segmentation is also insensitive to varying size of the exposed area in each layer.
- Using the edge-based active contour segmentation, the only significant differences were observed for the mean prediction variance in case of the $\delta_{Area}(z)$ deviation for the wall thickness effect, and in case of the $D_{TOT}(z)$ deviation for the illumination effect. However, despite such differences, the prediction variance was considerably lower than the one achieved with non-optimal active contour parameters.
- Moreover, when a non-optimal choice of active contour parameters is considered, i.e., the "ref" condition, both the illumination and the wall thickness have significant effects on the in-situ reconstruction accuracy, mainly on the prediction variance. A large effect of the illumination settings was also observed on the RMS of the deviation from the ground truth when the $\delta_{Area}(z)$ deviation was applied.

These results highlight the importance of fine tuning the active contour parameters to enhance the in-situ reconstruction. In this study, founded on experimental results gathered for gyroid structures with two different wall thicknesses and in two different illumination settings, a purely edge-based segmentation resulted to be the optimal choice. Interestingly, it made the in-situ geometry reconstruction not only more accurate than non-optimal choices of active contour parameters, but also more robust to changes in the illumination condition and in the wall thickness of the manufactured part.

Such higher robustness can be explained as follows. Illumination changes mainly affect the absolute intensity values rather than the relative contrast at object boundaries. This results into global offsets rather than local differences. Indeed, uniform changes in brightness/illumination tend to shift the whole pixel intensity histogram up or down. Because of this, region-based methods are more sensitive to such variations. Moreover, if illumination varies spatially, pixel intensity patterns are less homogeneous both inside and outside the contour, making region-based segmentation less effective. Edge-based active contours, on the contrary, evolve toward locations with strong image gradients, which are less affected by a change of illumination conditions from dark field to diffused light. Edges remained visible as intensity transitions, allowing the edge-based segmentation converging to a more accurate and robust reconstruction.

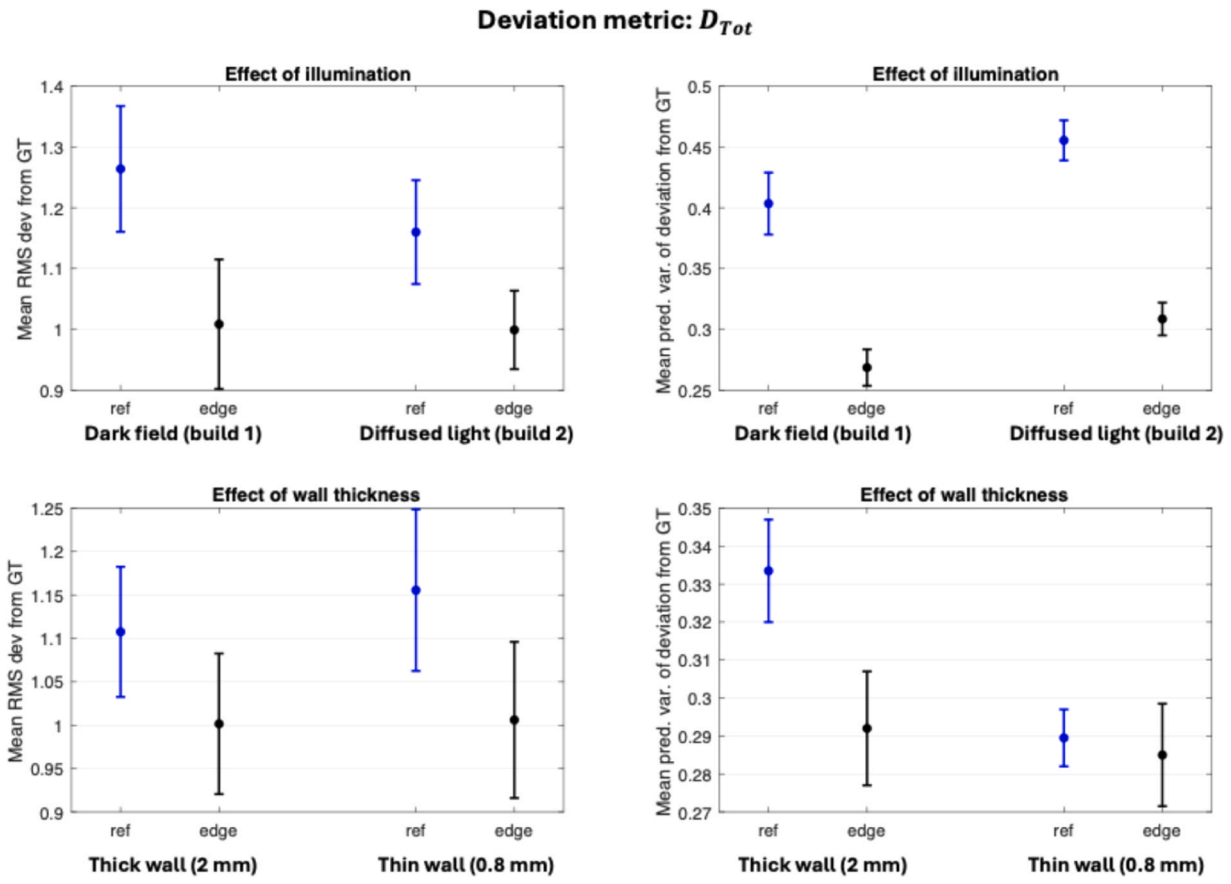

Fig. 9. – 95% confidence intervals for the effect of the different illumination settings and the different lattice wall thickness on the mean RMS and the prediction variance using the $D_{TOT}(z)$ deviation for different choices of the active contour parameters (ref, edge).

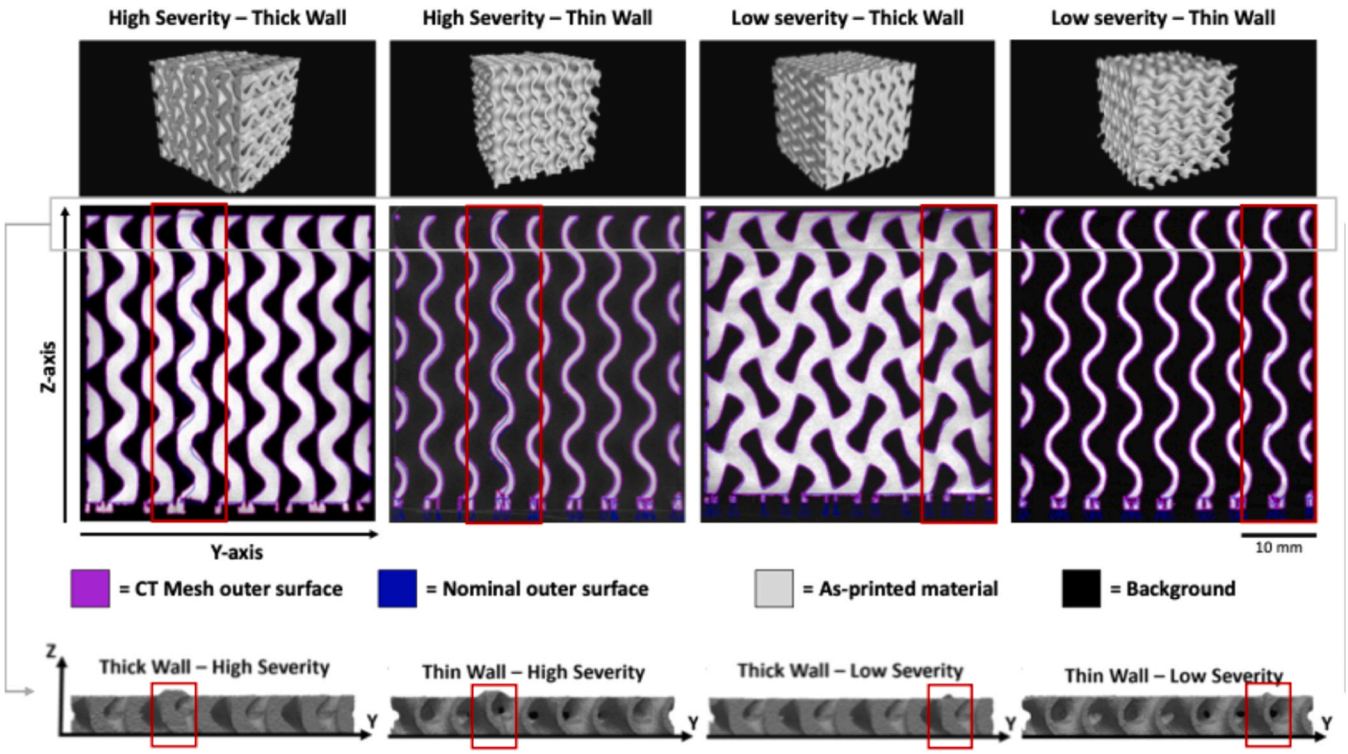

Fig. 10. – X-ray CT reconstruction of structures affected by low and high severity defects, with sections that highlight the presence of the deviation.

3.2. In-situ defect detection

Fig. 10 shows the geometrical deviations in the built structures produced by the artificially introduced anomalies in build 2. Along the lines affected by the recoater damage, a superelevation (or swelling) of the material was observed, because of a locally higher thickness of powder compared to the surroundings.

Fig. 11 shows an example of in-situ powder bed images where the local discontinuity caused by the damaged recoated is highlighted. A local variation in the pixel intensity is visible, especially in the presence of thick wall structures, where the solidified area affected by the anomaly is larger.

Fig. 12 shows the 1-D deviation profiles fitted via the proposed WLS method for gyroid structures in build 2, where different colors are used for unit cells not affected by the defect (green) and those affected by the defect (magenta). Different panels refer to different defect severities, different wall thicknesses, and different metrics to quantify the deviation from the nominal. In addition to the deviation metrics $\widehat{\delta}_{Area}(z)$ and $\widehat{D}_{tot}(z)$, Fig. 12 also shows the deviation profiles for the excess of material, $\widehat{D}_{excess}(z)$, and for the lack of material, $\widehat{D}_{deficit}(z)$. The effect of the defect is clear in the high severity case, for both the thin and thick wall structures. The difference between defect-free and defective cells is more evident in the $\widehat{\delta}_{Area}(z)$ deviation pattern than the $\widehat{D}_{tot}(z)$ one. However, when splitting the $\widehat{D}_{tot}(z)$ deviation from the nominal into its two complementary contributions, $\widehat{D}_{excess}(z)$ and $\widehat{D}_{deficit}(z)$, the effect of the defect is highly emphasized in the $\widehat{D}_{excess}(z)$ profiles. Indeed, the defect caused a local oversize of the structure, which is clearly captured by $\widehat{\delta}_{Area}(z)$ and $\widehat{D}_{excess}(z)$. In the presence of the low severity defect, the effect on the deviation profiles is visible in the thin wall structure, while for the thick wall structure the defective cells are hardly separable from the defect-free ones.

The summary of the defect detection performance in terms of both false positive (FP) and true positive (TP) rates is shown in Table 3. In this case, two different alarm rules were compared, i.e., one where an alarm is signaled if the deviation violates the control limits in at least $p = 1$ layer, and one where an alarm is signaled if the deviation violates the limits for at least $p = 5$ consecutive layers.

Table 3 shows that all defects can be detected in-situ with a TP rate of 100% apart from the low severity one in the presence of a thick wall structure. The control chart that yields the highest detection power is the one based on $\widehat{D}_{excess}(z)$. Indeed, the type of induced defect produced a local excess of material. Thus, splitting the deviation in two monitored quantities that separately capture the excess and the lack of material from the nominal shape, allows enhancing unidirectional shifts like the one here investigated. The control chart based on $\widehat{D}_{tot}(z)$ is less effective, as it adds both positive and negative discrepancies from the nominal, mitigating the effect that only entails the positive shift. The control chart based on $\widehat{\delta}_{Area}(z)$ is more effective than the one based on $\widehat{D}_{tot}(z)$, but not that effective as the one based on $\widehat{D}_{excess}(z)$. In some cases, due to the larger natural variability of the $\widehat{\delta}_{Area}(z)$ deviation profiles, some false positives are signaled. Setting the minimum number of control limit violations in consecutive layers before an alarm to $p = 5$ was not sufficient to avoid all such false positives.

4. Discussion

Several studies focused on the use of image segmentation methods applied to post-exposure powder bed images to i) reconstruct the geometry of the solidified layer, ii) compare it with the nominal shape, and iii) automatically detect anomalous deviations. Such methods have been tested in different laboratory and industrial implementations. Specific attention has been devoted to the influence of illumination settings on the reconstruction accuracy, but limited attention has been devoted to the tuning of active contour parameters, and the significance of their choice in real experimental conditions. The presented results highlighted that adopting tuned parameters significantly improve the in-situ reconstruction accuracy as well as the natural variability of the reconstruction itself. They also showed that under these experimental conditions, a purely edge-based active contour formulation is insensitive to variations of the illumination settings and to different lattice wall thickness.

Several factors may influence the intrinsic properties of powder bed images depending on the adopted imaging setup, and those properties impose the choice for appropriate parameters of image segmentation algorithms. Edge strength and pixel intensity homogeneity play a central role in determining the optimal choice. Generally speaking, there is no "universal" optimal set of parameters as changes in illumination, contrast, noise level, spatial resolution, and target object size/geometry possibly affect both gradient strength and region properties.

However, edge-based active contours have the advantage of not relying on pixel intensity distributions or pixel intensity homogeneity assumptions. Indeed, they showed robustness to varied factors. Generally speaking, purely edge-based active contour models may provide high accuracy in reconstructing the contour of solidified regions when well-defined intensity gradients are present at the melt boundary. Under

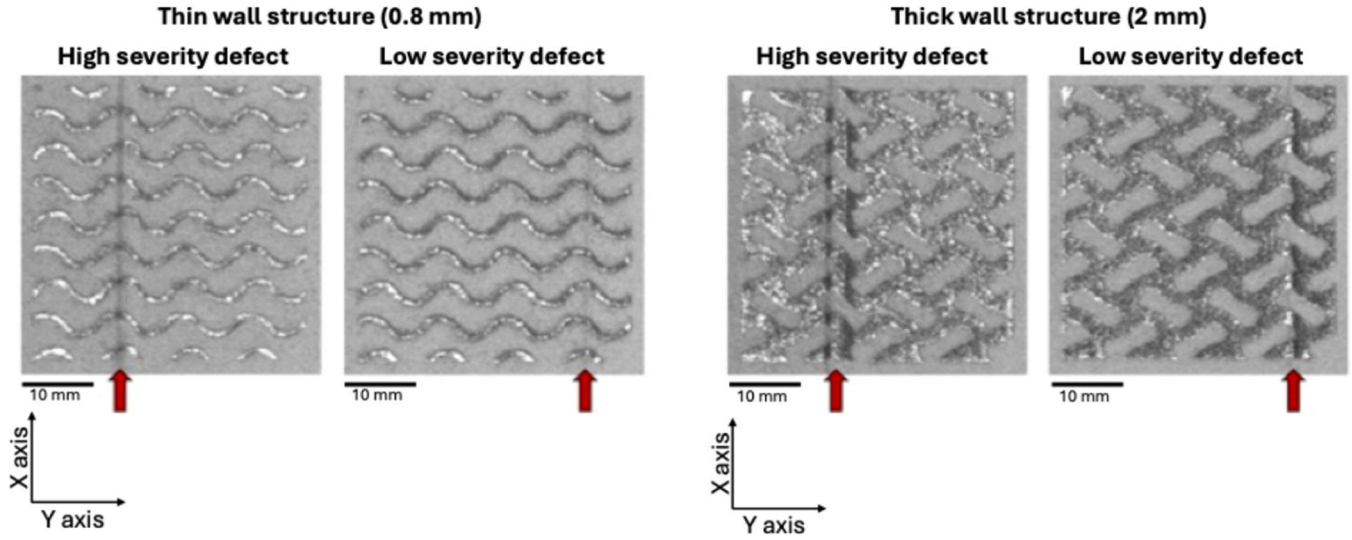

Fig. 11. – Examples of in-situ powder bed images of the structures affected by the low and high severity defects.

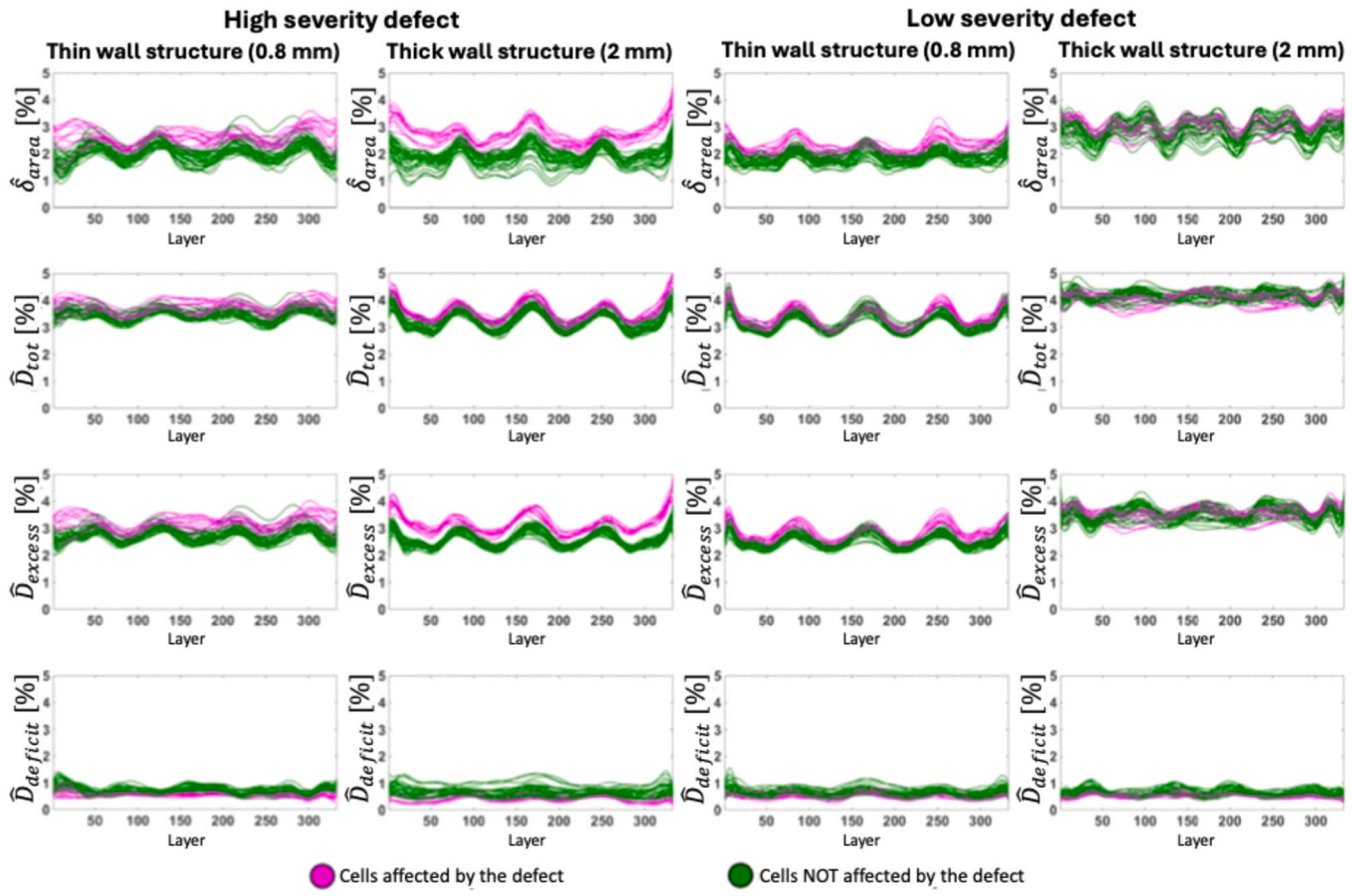

Fig. 12. – WLS fitted deviation profiles for gyroid structures affect by low and high severity defects; panels on different rows show profiles resulting from the selection of different deviation metrics; different colors are used to distinguish defect-free unit cells from defective ones.

Table 3 –
In-situ defect detection performances in terms of FP and TP.

Defect severity	Wall thickness	Deviation metric	FP (%)	TP (%)	FP (%)	TP (%)
			$p = 1$		$p = 5$	
Low	Thin	$\hat{\delta}_{Area}(z)$	0	56.3	0	50.0
		$\hat{D}_{tot}(z)$	0	12.5	0	12.5
		$\hat{D}_{excess}(z)$	**0**	**100**	**0**	**100**
	Thick	$\hat{\delta}_{Area}(z)$	0	0	0	0
		$\hat{D}_{tot}(z)$	0	12.5	0	12.5
		$\hat{D}_{excess}(z)$	**0**	**25.0**	**0**	**25.0**
High	Thin	$\hat{\delta}_{Area}(z)$	2.0	100	2.0	100
		$\hat{D}_{tot}(z)$	0	18.8	0	18.8
		$\hat{D}_{excess}(z)$	**0**	**100**	**0**	**100**
	Thick	$\hat{\delta}_{Area}(z)$	4.1	100	2.0	100
		$\hat{D}_{tot}(z)$	0	37.5	0	37.5
		$\hat{D}_{excess}(z)$	**2.0**	**100**	**0**	**100**

such conditions, the solidified contour typically exhibits sharp transitions with respect to the surrounding powder, allowing edge-driven formulations to precisely localize boundaries. This condition was observed in the powder-bed images analyzed in the present study with both illumination settings. When similar imaging conditions are met in other industrial implementations, edge-based active contours are therefore expected to provide accurate results. In more challenging scenarios where edge information is degraded (e.g., due to poor image quality, severe illumination inhomogeneities, surface reflectivity variations, etc.), purely edge-based approaches may become less effective. In such cases, region-based or hybrid formulations may offer improved robustness. The proposed calibration procedure is designed to support the selection of the most suitable active contour configuration under varying image quality and illumination conditions encountered in L-PBF applications.

Nonetheless, active contours involve other tuning parameters, like sigmoid function parameters (α_{sig} and β_{sig}) as well as the "balloon" parameter that penalizes the direction shrinkage and expansion of the contour in successive iterations. Regarding industrial implementation, fine tuning of all parameters may be considered, aiming to determine the optimal settings to be used in real production.

In the presence of a series production, a few copies of the same part can be used to tune the active contour parameters. Conversely, if the L-PBF process is adopted to produce a variety of geometries, ad-hoc calibration specimens can be designed and used to this aim, including the salient geometrical features of interest (e.g., thin walls, acute corners, overhang surfaces, etc.). In this study, X-ray CT of as-built parts was used as a ground truth. This is the only viable solution for calibration specimens that involve internal features that are not accessible with other methods. However, in case of simpler calibration shapes, different and more cost-efficient post-process geometry reconstruction methods can be used instead, e.g., optical or laser scanning of the manufactured part.

The study also highlighted the relevance of choosing appropriate deviation metrics. The ones investigated here represent just a limited set of a broad range of suitable quantities that can be computed in-situ. Metrics such as $\hat{D}_{tot}(z)$, which quantify the point-wise mismatch between nominal and reconstructed regions, provide a direct measure of geometric discrepancy and are therefore more suitable for in-situ monitoring and inspection applications. As discussed, these metrics

are more sensitive to misalignment errors, but they are also more effective in capturing localized deviations affecting the overlap between regions. In contrast, metrics such as $\widehat{\delta}_{Area}(z)$, which only depend on the total area mismatch, are inherently more robust to misalignment but may fail to capture local distortions that do not significantly affect the global area.

From a practical viewpoint, the selection of the deviation metric should be guided by the expected defect characteristics and by the dominant sources of variability. When accurate spatial registration can be ensured and localized defects are of primary concern, overlap-based metrics (e.g., $\widehat{D}_{tot}(z)$ or their directional decompositions) are preferable. Conversely, in scenarios where residual misalignment or imaging uncertainty is significant, more aggregated metrics such as $\widehat{\delta}_{Area}(z)$ may provide a better compromise and more stable monitoring performance.

A particularly relevant outcome of this study is that monitoring deviations affecting the intersection between the in-situ reconstructed region and the nominal one enables the decomposition of the deviation into two complementary "directional" descriptors, capturing excess and lack of material, respectively. This approach was shown to outperform non-directional metrics in detecting defects like local oversizing caused by recoating anomalies. We pointed out that the proposed $\widehat{D}_{tot}(z)$ metric and its directional variants share similarities with overlap-based distance measures that saturate when the two regions become disjoint. While this behavior is appropriate for defect detection, since complete lack of overlap already indicates a severe deviation, it does not capture the spatial separation between disjoint regions. An extension toward formulations suitable to incorporate spatial displacement, allowing the deviation metric to increase as the distance between regions grows, may be explored in future research.

Another relevant aspect regards the characterization of in-situ anomaly detection performance. Generally speaking, a rigorous estimation of the minimum detectable anomaly size at a given confidence level would require a Probability of Detection (PoD) analysis. Such an approach enables quantifying detection capability as a function of defect size and variability. A methodology describing how PoD analysis can be applied to in-situ image data for automated detection of geometrical and dimensional deviations was recently presented in Bugatti et al. [6]. In the present study, the limited number of defect severities (two levels) did not allow for a statistically meaningful Probability of Detection (PoD) analysis. Nevertheless, the integration of the proposed approach within a PoD framework represents a highly relevant direction for industrial application. Such an analysis could be conducted during the development and calibration phase to systematically assess detection limits, evaluate the suitability of the in-situ inspection system, and identify potential margins for improvement. These may arise from both the hardware side (e.g., camera selection, sensor placement, illumination conditions) and the image processing side (e.g., segmentation strategy and parameter tuning).

Apart from the in-situ defect detection capability, Fig. 12 showed that, despite the optimal choice of edge-based active contours, the pattern of 1-D deviation profiles may exhibit some variations from part to part. As an example, this was evident for the thick wall structure affected by the low severity defect in build 2. This part-to-part variability of profile patterns may be ascribed to location effects, since depending on the position of the part within the build, the solidified surface is captured at different angles, and it reflects light in a different way towards the camera. Such location-dependent variability affected in-situ collected data, but it did not reflect in the ground truth measurement. Such location effect, when present, may inflate the natural variability of deviation profiles and cause higher false alarm rates. The calibration of the image segmentation method represents one important way to enhance the robustness of the in-situ detection of geometrical (or dimensional) deviations, but it may be not sufficient to completely avoid the issue. To further reduce the natural variability of powder bed images more effective imaging methods may be explored and implemented. Tuning the lighting setup withing the build chamber can only partially mitigate this effect. A more effective solution would involve the use of powder bed imaging methods that minimize optical distortions and perspective errors while homogenising the light reflections over the whole build area. From this perspective, a blade-mounted imaging system may provide notable advantages with respect to standard powder bed cameras, also enabling a much higher spatial resolution. Examples can be found in Bugatti and Colosimo [5], and Tan Phuc and Seita [31]. A recent comparison of powder bed imaging methods to enhance the detection of in-situ geometrical deviations in L-PBF can be found in Bugatti et al. [6].

5. Conclusions

This study explored the influence of active contour parameters on the in-situ reconstruction performance, as regards the in-situ inspection and monitoring of geometrical deviations of lattice structures. It also highlighted the role played by the choice of deviation metrics in enhancing the reconstruction accuracy and improving the defect detection capacity. Despite the increasing attention devoted to in-situ monitoring of geometrical errors in L-PBF, these aspects have been poorly investigated in the literature so far. Salient results can be briefly summarized as follows:

- The tuning of active contour parameters significantly improves the in-situ reconstruction accuracy; to this aim, a calibration procedure that is easily implementable in industrial applications has been proposed;
- Edge-based active contour provides segmentation results that are robust both to variations of illuminations settings (from dark field to diffused light) and to part size (different lattice structure wall thickness);
- A proper choice of deviation metric may influence the natural variability of observed deviations in defect-free conditions and improve the in-situ detectability of actual defects;
- A directional deviation metric, specifically designed to detect an excess of material from the nominal geometry, allowed improving the in-situ detectability of observed defects.
- The selection of the monitoring metric should be aligned with the industrial specifications, accounting both for the type of defect to be detected and for the critical defect size relevant to the application. In this way, the metric directly reflects the inspection requirements of the intended implementation scenario

In-situ inspection of complex shapes like lattice structures, as well as in-process detection of geometrical deviations during the L-PBF process represent high TRL methods with a high potential for a direct implementation in industry. This study contributed to the definition of calibration and validation procedures that can be easily applied in production environments. Moreover, targeting in-situ imaging and segmentation methods that are insensitive to variations in the illumination conditions or part size/geometry is crucial to enhance in-situ geometry reconstruction accuracy and repeatability, especially for series production.

One ongoing development regards the extension of the experimental activity by including validation test cases involving different types and severity of real defects. The aim is to achieve a broader characterization of in-situ detection performances while quantitatively assessing the benefits and drawbacks of different deviation metrics and alternative monitoring schemes.

A further development regards the extension and scaling of the proposed method to more general types of part geometries. Indeed, the proposed approach applied to lattice structures with unit cells of the same size and shape. Going beyond the framework of structures with spatially repeating unit cells would require revising the way in which deviations are quantified and modelled. Different control charting

schemes have been proposed in Pagani et al. [27] and used in Bugatti et al. [6]. The calibration procedure proposed in this work is, in principle, independent of the specific deviation metric and alarm rule adopted for anomaly detection and can therefore be applied more generally across different monitoring frameworks. However, the tuning and adaptation of the method to lattice structures with spatially varying geometries remains an open aspect and is currently under investigation.

CRediT authorship contribution statement

Bianca Maria Colosimo: Writing – review & editing, Writing – original draft, Validation, Supervision, Methodology, Conceptualization. **Michael Dallmann:** Writing – review & editing, Supervision, Resources, Project administration, Investigation, Conceptualization. **Dimitrii Ertelthalner-Nikolaev:** Writing – review & editing, Supervision, Resources, Project administration, Investigation, Conceptualization. **Marco Grasso:** Writing – original draft, Validation, Methodology, Formal analysis, Data curation.

Declaration of Competing Interest

The authors declare that they have no known competing financial interests or personal relationships that could have appeared to influence the work reported in this paper.

Acknowledgements

The authors are grateful to Gioele Malacarne for his contribution in data organization and code adaptation to the present study.

Data availability

The data that has been used is confidential.

References

[1] M. Abdelrahman, E.W. Reutzel, A.R. Nassar, T.L. Starr, Flaw detection in powder bed fusion using optical imaging, Addit. Manuf. 15 (2017) 1–11.
[2] M. Aminzadeh, T. Kurfess, Vision-based inspection system for dimensional accuracy in powder-bed additive manufacturing, V002T04A042, in: International manufacturing science and engineering conference, 49903, American Society of Mechanical Engineers, 2016.
[3] ASTM Report, Strategic Guide: Additive Manufacturing in-situ monitoring technology readiness – findings and path forward for application in qualification and certification, ASTM International, Additive Manufacturing Center of Excellence, 2023.
[4] B.B. Avants, N.J. Tustison, M. Stauffer, G. Song, B. Wu, J.C. Gee, The insight toolkit image registration framework, Front. Neuroinform 8 (44) (2014).
[5] M. Bugatti, B.M. Colosimo, The intelligent recoater: A new solution for in-situ monitoring of geometric and surface defects in powder bed fusion, Addit. Manuf. Lett. 3 (2022) 100048.
[6] M. Bugatti, M. Grasso, B.M. Colosimo, In-situ monitoring of geometrical defects in laser powder bed fusion: probability of detection across defect sizes and sensor architectures, Prog. Addit. Manuf. (2025) 1–12.
[7] F. Caltanissetta, M. Grasso, S. Petro, B.M. Colosimo, Characterization of in-situ measurements based on layerwise imaging in laser powder bed fusion, Addit. Manuf. 24 (2018) 183–199.
[8] Colosimo et al. 2024,
[9] B.M. Colosimo, F. Garghetti, M. Grasso, L. Pagani, On-line inspection of lattice structures and metamaterials via in-situ imaging in additive manufacturing, Addit. Manuf. 95 (2024) 104538.
[10] B.M. Colosimo, F. Garghetti, L. Pagani, M. Grasso, A novel method for in-process inspection of lattice structures via in-situ layerwise imaging, Manuf. Lett. 32 (2022) 67–72.
[11] A. Donmez, J. Fox, F. Kim, B. Lane, M. Praniewicz, V. Tondane, J. Weaver, P. Witherell, In-process monitoring and non-destructive evaluation for metal additive manufacturing. NIST Internal Report, NIST IR 8538, 2024, https://doi.org/10.6028/NIST.IR.8538.
[12] A. Du Plessis, S.G. le Roux, J. Waller, P. Sperling, N. Achilles, A. Beerlink, P. Konrad, Laboratory X-ray tomography for metal additive manufacturing: Round robin test, Addit. Manuf. 30 (2019) 100837.
[13] R. Fabbri, L.D.F. Costa, J.C. Torelli, O.M. Bruno, 2D Euclidean distance transform algorithms: A comparative survey, ACM Comput. Surv. (CSUR) 40 (1) (2008) 1–44.
[14] F.G. Fischer, N. Birk, T.G. Lücke, N. Praetzsch, Detection of the Part Geometry in Laser Powder Bed Fusion Using Layer-Wise Images, Prog. Addit. Manuf. 2021 (2022) 86–100.
[15] A. Gaikwad, F. Imani, P. Rao, H. Yang, E. Reutzel, Design rules and in-situ quality monitoring of thin-wall features made using laser powder bed fusion, V001T01A039, in: International Manufacturing Science and Engineering Conference, 58745, American Society of Mechanical Engineers, 2019.
[16] M. Grasso, A. Remani, A. Dickins, B.M. Colosimo, R.K. Leach, In-situ measurement and monitoring methods for metal powder bed fusion: an updated review, Meas. Sci. Technol. 32 (11) (2021) 112001.
[17] R. Hartley, A. Zisserman, Multiple view geometry in computer vision, Cambridge university press, 2003.
[18] P. He, K. Zhong, X. Liu, G. Zhou, C. Wang, Q. Wei, Z. Li, A phase-guided method for extracting the contour of the fusion area in laser powder bed fusion, in: Seventh International Conference on Optical and Photonic Engineering (icOPEN 2019), 11205, International Society for Optics and Photonics, 2019, p. 112051H.
[19] M. Helou, S. Kara, Design, analysis and manufacturing of lattice structures: an overview, Int. J. Comput. Integr. Manuf. 31 (3) (2018) 243–261.
[20] I. Jahr, Lighting in machine vision, Handb. Mach. Vis. (2006) 73–203.
[21] S. Krig, Computer Vision Metrics: Survey, Taxonomy, and Analysis of Computer Vision, Visual Neuroscience, and Visual AI, Springer Nature, 2025.
[22] Z. Li, X. Liu, S. Wen, P. He, K. Zhong, Q. Wei, S. Liu, In-situ 3D monitoring of geometric signatures in the powder-bed-fusion additive manufacturing process via vision sensing methods, Sensors 18 (4) (2018) 1180.
[23] S. Liu, Y. Peng, A local region-based Chan–Vese model for image segmentation, Pattern Recognit. 45 (7) (2012) 2769–2779.
[24] R. McCann, M.A. Obeidi, C. Hughes, É. McCarthy, D.S. Egan, R.K. Vijayaraghavan, D. Brabazon, In-situ sensing, process monitoring and machine control in Laser Powder Bed Fusion: A review, Addit. Manuf. 45 (2021) 102058.
[25] D.C. Montgomery, Statistical quality control, 7, Wiley, New York, 2012.
[26] S. Osher, R. Fedkiw, K. Piechor, Level set methods and dynamic implicit surfaces, Appl. Mech. Rev. 57 (3) (2004). B15-B15.
[27] L. Pagani, M. Grasso, P.J. Scott, B.M. Colosimo, Automated layerwise detection of geometrical distortions in laser powder bed fusion, Addit. Manuf. 36 (2020) 101435.
[28] T. Saini, P.S. Shiakolas, In-situ Active Contour-Based Segmentation and Dimensional Analysis of Part Features in Additive Manufacturing, J. Manuf. Mater. Process. 9 (3) (2025) 102.
[29] S. Soomro, A. Munir, K.N. Choi, Hybrid two-stage active contour method with region and edge information for intensity inhomogeneous image segmentation, PloS One 13 (1) (2018) e0191827.
[30] R. Szeliski, Image alignment and stitching. Computer Vision, Springer, Cham, 2022, pp. 401–441.
[31] L. Tan Phuc, M. Seita, A high-resolution and large field-of-view scanner for in-line characterization of powder bed defects during additive manufacturing, Mater. & Des. 164 (2019) 107562.
[32] X. Wu, Y. Su, J. Shi, Perspective of additive manufacturing for metamaterials development, Smart Mater. Struct. 28 (9) (2019) 093001.
[33] Y. Zhang, W. Yan, Applications of machine learning in metal powder-bed fusion in-process monitoring and control: status and challenges, J. Intell. Manuf. 34 (6) (2023) 2557–2580.
[34] J. zur Jacobsmühlen, J. Achterhold, S. Kleszczynski, G. Witt, D. Merhof, In-situ measurement of part geometries in layer images from laser beam melting processes, Prog. Addit. Manuf. 4 (2) (2019) 155–165.